Research Square

Preprints are preliminary reports that have not undergone peer review.
They should not be considered conclusive, used to inform clinical practice,
or referenced by the media as validated information.

Target-tissue photon absorption enables precision optical-dose planning for photobiomodulation

Ting Li

liting@bme.cams.cn

Chinese Academy of Medical Sciences & Peking Union Medical College

Zemeng Chen

Institute of Biomedical Engineering, Chinese Academy of Medical Sciences & Peking Union Medical College

Ming Li

Xuanwu Hospital, Capital Medical University

Pei Wang

Institute of Biomedical Engineering, Chinese Academy of Medical Sciences & Peking Union Medical College

Jingjing Jiang

Computational Optical Imaging Group, Biomedical Optics Research Laboratory, Department of Neonatology, University Hospital Zurich, University of Zurich https://orcid.org/0000-0002-3983-7647

Felix Wang

School of Environmental Science and Engineering, Tianjin University

Bowen Zhang

Institute of Biomedical Engineering, Chinese Academy of Medical Sciences & Peking Union Medical College

Xinzhe Cao

Institute of Biomedical Engineering, Chinese Academy of Medical Sciences & Peking Union Medical College

Lin Z. Li

3 Britton Chance Laboratory of Redox Imaging and Laboratory of Molecular Imaging, Department of Radiology, Perelman School of Medicine, University of Pennsylvania https://orcid.org/0000-0001-9447-7982

Erxi Wu

Department of Neurosurgery, Baylor Scott & White Medical Center https://orcid.org/0000-0002-1680-3639

Jason H. Huang

Department of Neurosurgery, Baylor Scott & White Medical Center

Article

Keywords: Photobiomodulation, Optical dosimetry, Optical imaging, Photon absorption, Spinal cord injury

Posted Date: November 24th, 2026

DOI: https://doi.org/10.21203/rs.3.rs-11539638/v1

License: This work is licensed under a Creative Commons Attribution 4.0 International License.
Read Full License

Additional Declarations: There is no conflict of interest

Target-tissue photon absorption enables precision optical-dose planning for photobiomodulation

Zemeng Chen[1†], Ming Li[2†], Pei Wang[1], Jingjing Jiang[3], Felix Wang[4-5], Bowen Zhang[1], Xinzhe Cao[1], Lin Z. Li[6], Erxi Wu[7-8], Jason H. Huang[7-8], Ting Li[1, *]

1 Biomedical Engineering Institute, Chinese Academy of Medical Sciences and Peking Union Medical College, Tianjin, 300192, China

2 Neuro-Cardiovascular Research Center, Xuanwu Hospital, Capital Medical University

3 Computational Optical Imaging Group, Biomedical Optics Research Laboratory, Department of Neonatology, University Hospital Zurich, University of Zurich, Zurich, Switzerland

4 School of Environmental Science and Engineering, Tianjin University, Tianjin, China

5 Department of Biosystems, KU Leuven, Leuven, Belgium

6 Britton Chance Laboratory of Redox Imaging, Department of Radiology, Perelman School of Medicine University of Pennsylvania, Philadelphia, PA 19104, USA

7 Department of Neurosurgery, Baylor Scott & White Medical Center, Temple, USA

8 Department of Neurosurgery, Baylor College of Medicine, Temple, Texas, USA

* Correspondence should be addressed to T.L. (liting@bme.cams.cn).

† These authors contributed equally to this work.

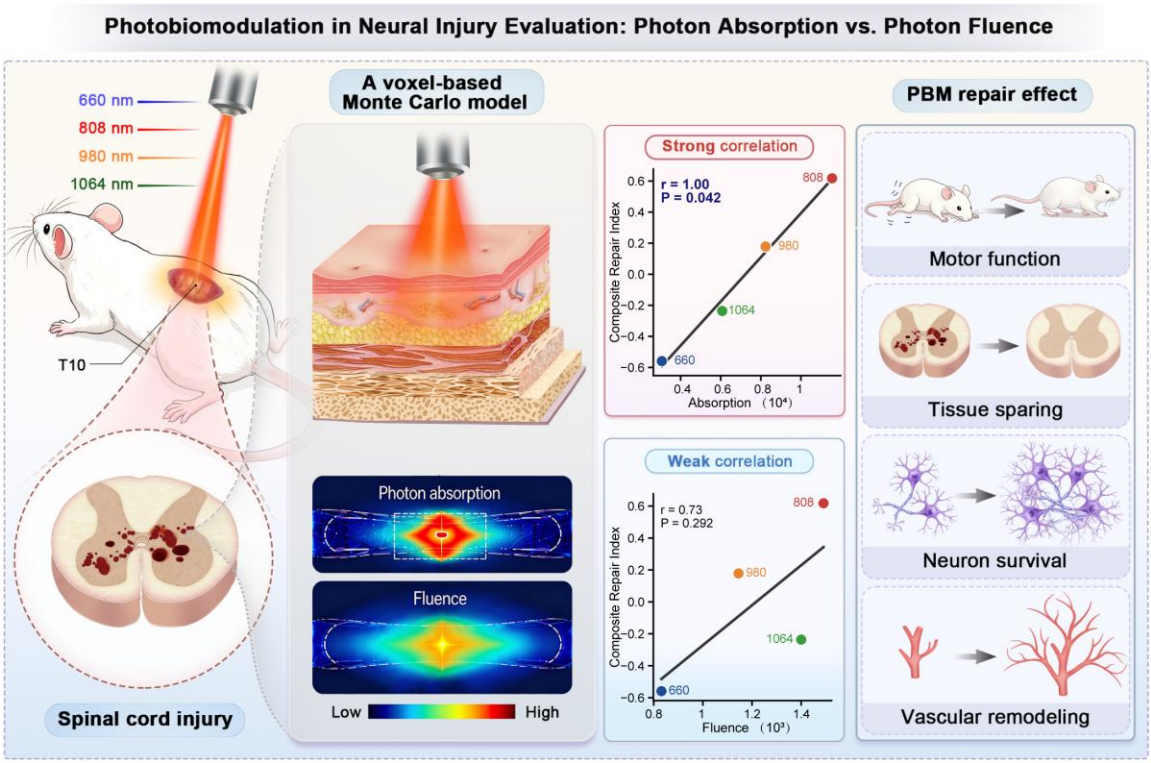

Graphical abstract | Target-level optical dose for precision photobiomodulation. Light-based interventions are conventionally dosed according to device emission or tissue-surface parameters, whereas biological responses depend on optical energy received and absorbed by target tissues. We evaluate computed tissue photon absorption as a target-level dose metric. Voxel-based light-transport computation converts wavelength-specific irradiation into target-tissue photon fluence (propagated light) and photon absorption (locally deposited optical energy). A rat T10 compression SCI study serves as a deep-tissue test case for comparing which optical quantity tracks time-resolved repair more closely.

Abstract

As photobiomodulation (PBM) moves toward broader clinical use, precise light delivery is increasingly feasible. Yet the target-tissue optical quantity that should guide biologically meaningful dose control remains uncertain. Computational dosimetry commonly uses fluence to characterize internal light exposure, although local optical absorption can also be estimated. We compared model-derived fluence and relative integrated absorption with matched functional and tissue-level outcomes in a rat model of spinal cord injury. An anatomy-resolved voxel Monte Carlo model estimated both quantities in the same spinal cord region for four illumination conditions delivered at the same prescribed surface dose. Across functional, histological, neuronal and vascular readouts at 1, 7 and 14 days, absorption showed larger absolute correlations than fluence in 35 of 37 evaluable endpoint-by-time-point comparisons. It also showed a stronger association with a cross-time Composite Repair Index. Exploratory reanalyses of published traumatic brain injury and healthy-human forearm PBM data showed a similar directional pattern. These findings distinguish estimating light delivery from identifying an optical descriptor associated with biological response. They identify target-tissue absorption as a candidate for further evaluation in PBM dosimetry. The evidence remains associative and is based on four wavelength-level conditions and relative, uncalibrated model outputs. It does not yet establish absorption-guided clinical dose control.

Keywords: Photobiomodulation; Optical dosimetry; Optical imaging; Photon absorption; Spinal cord injury

Introduction

As photobiomodulation (PBM) advances toward broader clinical application, precise and reproducible optical-dose control is becoming increasingly important.[1-3] Although wavelength, irradiance, radiant exposure and exposure time can be prescribed at the source, these settings do not establish how much light reaches or is deposited within a deep biological target. Tissue geometry, scattering and absorption redistribute incident light, prompting wider use of anatomy-informed Monte Carlo models to estimate internal optical exposure.[4-7] This progress has improved the characterization of light transport, but a more fundamental question for treatment planning remains: which target-level optical quantity should guide dose evaluation when the aim is a reproducible biological response? Fluence and fluence rate describe the propagated optical field, whereas local absorption reflects energy deposited in tissue and depends additionally on its absorption properties.

Recent studies illustrate how fluence-based estimates have been used in practice. Yuan et al. simulated age-related differences in transcranial light delivery to characterize internal exposure.[8] Using MRI-derived anatomy from 18 individuals, Yaroslavsky et al. calculated oral-mucosal fluence rate for extraoral PBM and used it to derive illumination times for a predefined target radiant exposure. Total tissue thickness substantially affected the predicted mucosal fluence rate.[9] Chang et al. combined diffuse-reflectance spectroscopy, anatomical features and deep learning to estimate fluence rate in prefrontal brain targets. This reduced the error relative to simulated reference values from approximately 49% under a constant-scalp-irradiance assumption to 13%.[10] More recently, Zhang et al. used voxel Monte Carlo simulations to identify transcranial incidence sites and propose source-power ratios based on brain-parenchymal fluence.[11] Girasol et al. integrated experimentally characterized laser beams and skin optical properties into Monte Carlo calculations and identified beam radius as a major determinant of subsurface fluence rate.[12] Enam et al. combined micro-CT-informed skull simulations with phantom measurements to compare transcranial device transmission and detector-plane fluence.[13] These studies substantially advanced optical prediction and treatment-device assessment, but they did not establish that fluence explains measured therapeutic responses better than absorption.

Absorption itself is not a new output of computational light transport. In addition to fluence rate, Yaroslavsky et al. reported spatial absorbed-power distributions, yet their treatment-time calculation remained anchored to the prescribed mucosal radiant-exposure target.[9] Van Lankveld et al. extended human-head Monte Carlo dosimetry to light penetration and cortical energy accumulation during transcranial and intranasal PBM. They showed that optical power, illumination route and skin-associated absorption can markedly alter energy reaching or accumulating in particular brain regions, but did not test either optical descriptor against corresponding treatment outcomes.[14] Experimental photobiology further cautions against equating administered fluence with a fixed biological effect. Amaroli et al. exposed isolated mitochondria to 810 nm light at the same incident radiant exposure of 30 J cm−2 but varied power and exposure duration; ATP-related responses differed across the conditions.[15] This result challenges equivalence based on surface dose alone, although it does not demonstrate that bulk tissue absorption outperforms internal fluence as a correlate of therapeutic benefit. More broadly, biphasic dose responses have been reported in PBM experiments, underscoring the limits of a single exposure parameter.[16]

The distinction between light delivery and biological dose is not merely semantic. Local absorbed power density is proportional to fluence rate multiplied by the tissue absorption coefficient, so the quantities are physically related but need not change in proportion across heterogeneous tissues and illumination conditions.[4,7] Recent work on optical penetration and dose estimation has emphasized how strongly tissue-dependent transport influences internal exposure.[17] At the cellular level, photobiological responses begin with photon absorption by endogenous photoacceptors, followed by mitochondrial and other signaling processes.[18-20] Yet the integrated absorption calculated for an anatomical region includes energy deposited in blood, water and other constituents, not only in the molecules that initiate PBM signaling. Thus neither the physical relation between fluence and absorption nor the biological requirement for photon absorption establishes that bulk tissue absorption is necessarily the better therapeutic dose metric. To choose a biologically informative target-dose descriptor, both quantities must be computed for the same target and evaluated against the same measured outcomes.

To test this unresolved dose-metric question in a deep and optically heterogeneous target, we used a rat model of T10 spinal cord injury. Externally applied light must pass through skin, adipose tissue, muscle and bone before reaching the injured cord, while functional, histological, neuronal and vascular measurements offer complementary readouts of repair. Our earlier anatomy-resolved spinal cord Monte Carlo study mapped fluence and absorption but did not compare them with matched biological outcomes.[21] Here, we estimated both optical quantities in the same spinal cord region under four irradiation conditions with matched prescribed surface doses. Wavelength was used to generate distinct internal exposures rather than to propose a wavelength-selection rule. We then compared each metric with recovery at 1, 7 and 14 days after injury. To our knowledge, this is the first systematic paired assessment of model-derived target fluence and total absorption against multiple matched repair outcomes in this deep-tissue PBM injury setting. Absorption showed stronger and more consistent associations with recovery than fluence under the investigated conditions, and exploratory reanalyses of published traumatic brain injury and healthy-human forearm datasets showed a similar directional pattern.[22,23] The contribution is twofold: an empirical test of which internal optical descriptor is more closely related to biological outcomes, and an anatomy-resolved computational means of estimating the candidate descriptor. This approach advances dose-metric evaluation, while absorption-guided clinical prescription remains to be validated.

Results

Anatomy-resolved estimation of target-tissue optical exposure

We combined anatomy-resolved light-transport computation with measurements of recovery after T10 compression injury (Fig. 1). Fluence and absorption were calculated for four illumination conditions and extracted from a common spinal cord region of interest (ROI). The resulting optical quantities were compared with functional, histological, neuronal and vascular readouts.

BBB score, CatWalk cadence and spontaneous voiding were used to assess functional recovery. H&E, Nissl, NeuN and CD31 measurements characterized tissue damage,

neuronal structure and vascular-associated morphology. Together, these outcomes allowed the two optical descriptors to be compared across several aspects of repair.

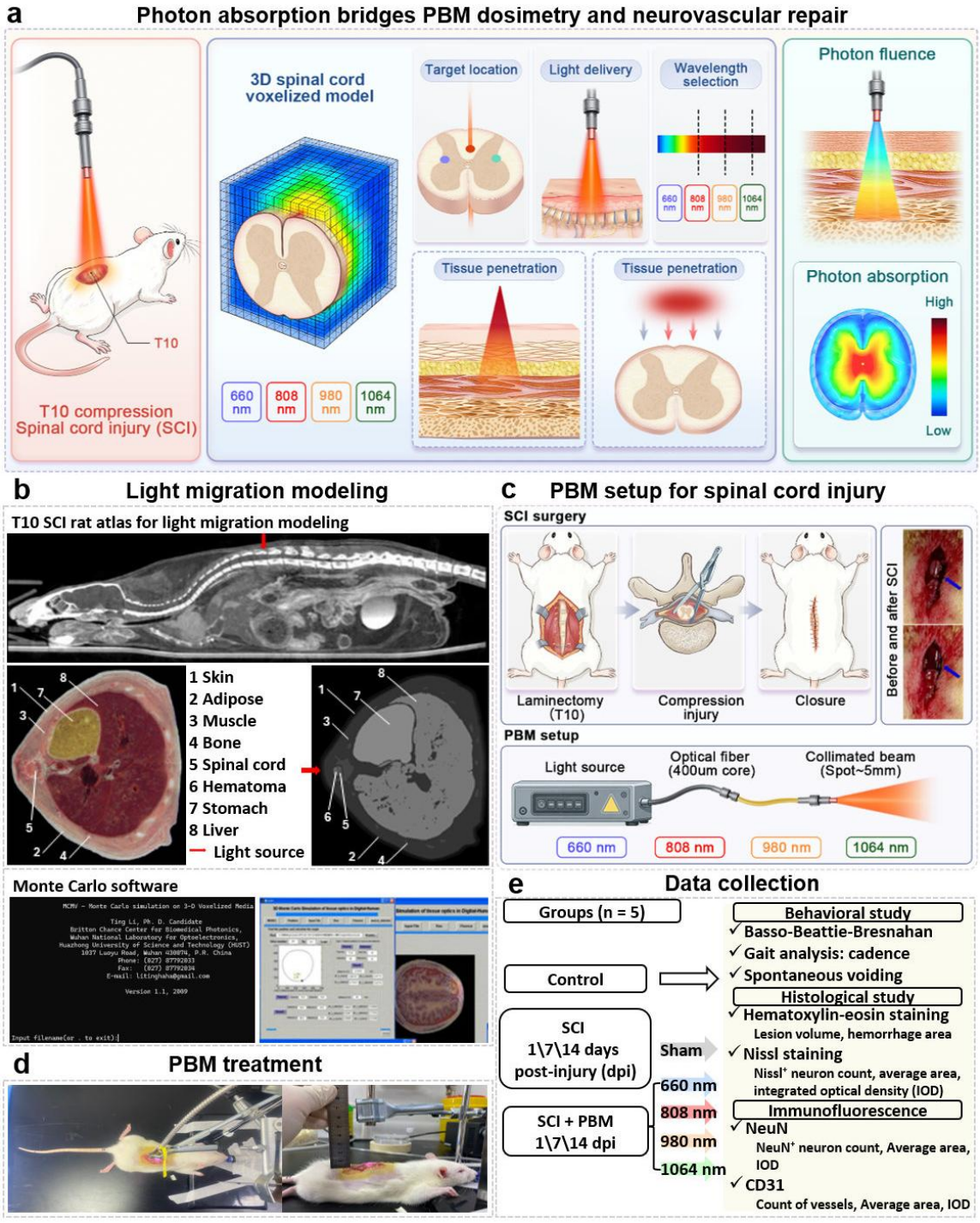

Fig. 1 | Framework for evaluating target-tissue optical descriptors. (a) Conceptual workflow linking prescribed light delivery to computed target optical variables and

matched biological outcomes. (b) Anatomical light-transport modelling workflow, including the voxelized T10 rat thoracic model and computational interface. (c) Experimental procedure for T10 compression SCI and wavelength-specific PBM delivery. (d) Representative in vivo PBM irradiation. (e) Experimental groups, endpoint schedule and biological data collection. This framework distinguishes propagated photon fluence from locally absorbed optical energy within the target ROI.

Distinct target distributions of fluence and absorption

The voxel model represented light transport through skin, adipose tissue, muscle, bone, spinal cord, hematoma and nearby visceral tissues (Fig. 1b). Fluence and absorption showed related but distinct spatial patterns in the same geometry (Fig. 2). Fluence described the local propagated optical field, while absorption reflected photon-weight losses assigned to the tissues traversed.

Depth-dependent and transverse and longitudinal profiles further resolved differences between the computed quantities (Fig. 2). ROI-integrated fluence and absorption did not change in the same proportion across illumination conditions. Voxel-threshold plots also described the spatial coverage of each metric, applying common thresholds across illumination inputs *within each metric* rather than interpreting identical numerical thresholds for fluence and absorption as physically equivalent. Fluence therefore should not be treated as a direct numerical substitute for absorbed energy. This provided the basis for testing how closely each measure corresponded to the observed recovery outcomes, rather than selecting conditions solely by light penetration (Fig. 2p,q).

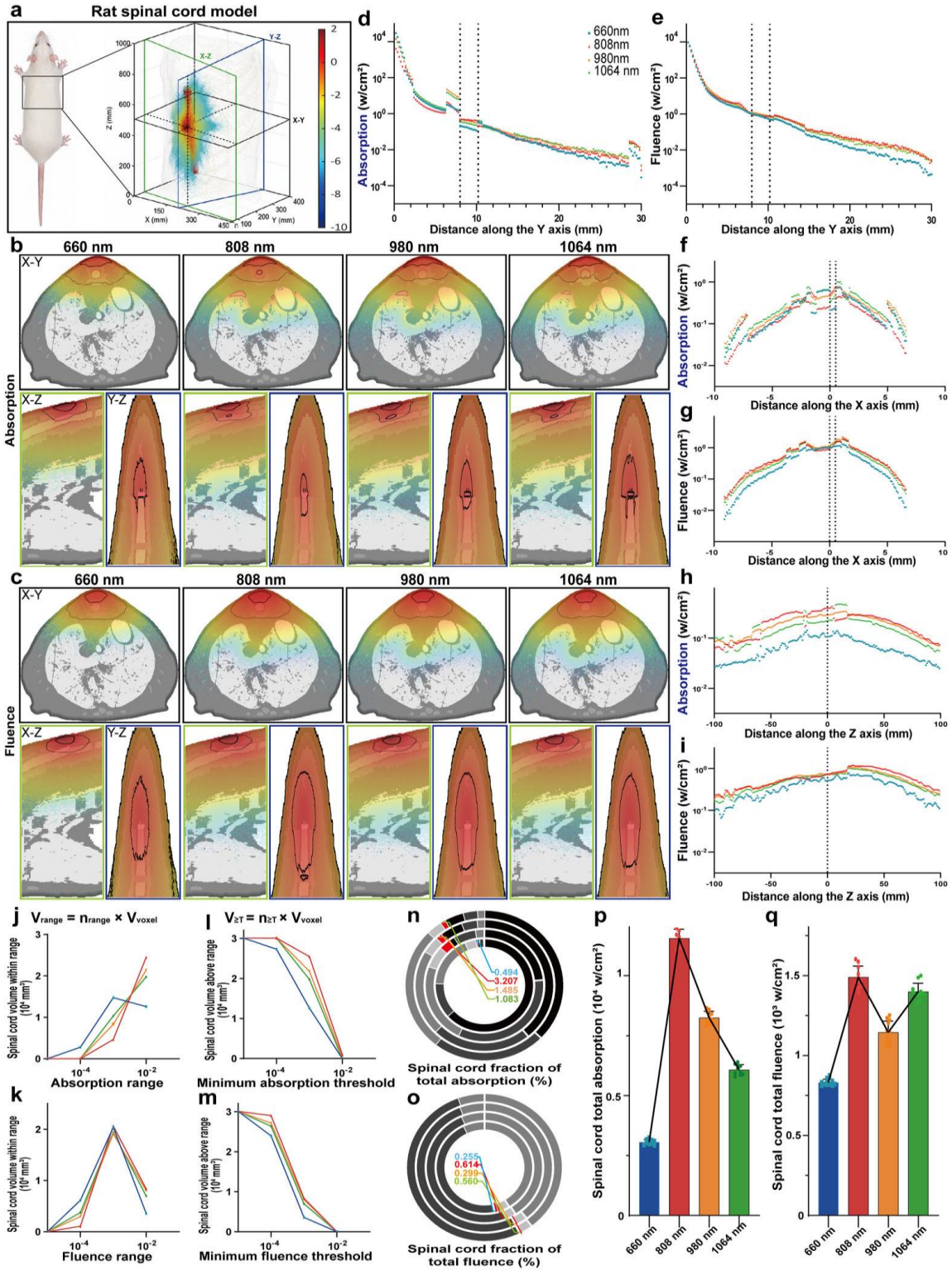

Fig. 2 | Anatomical light-transport computation resolves tissue-level light propagation and absorption. (a) Three-dimensional rat spinal cord model and analysis planes. (b,c) Log-transformed absorption and fluence maps at 660, 808, 980 and 1064 nm. (d-i) Depth,

transverse and longitudinal profiles. (j-m) Voxel-volume distributions and cumulative volume-threshold curves; Vrange denotes spinal cord volume within each intensity range, and V>=t denotes spinal cord volume above each threshold. (n,o) Spinal cord fractions of total tissue absorption and fluence. (p,q) Integrated spinal cord absorption and fluence across wavelengths.

Functional outcomes and target-tissue absorption

SCI reduced hindlimb movement, gait performance and spontaneous voiding, with varying improvement after PBM treatment (Fig. 3). At 14 days after injury, all three functional endpoints could be compared with the computed optical quantities. Their absolute correlations were generally larger for absorption than for fluence, most clearly for cadence ($r = 0.97$, $P = 0.031$). The Williams tests did not detect significant differences between the paired correlations for individual endpoints (Supplementary Table 32).

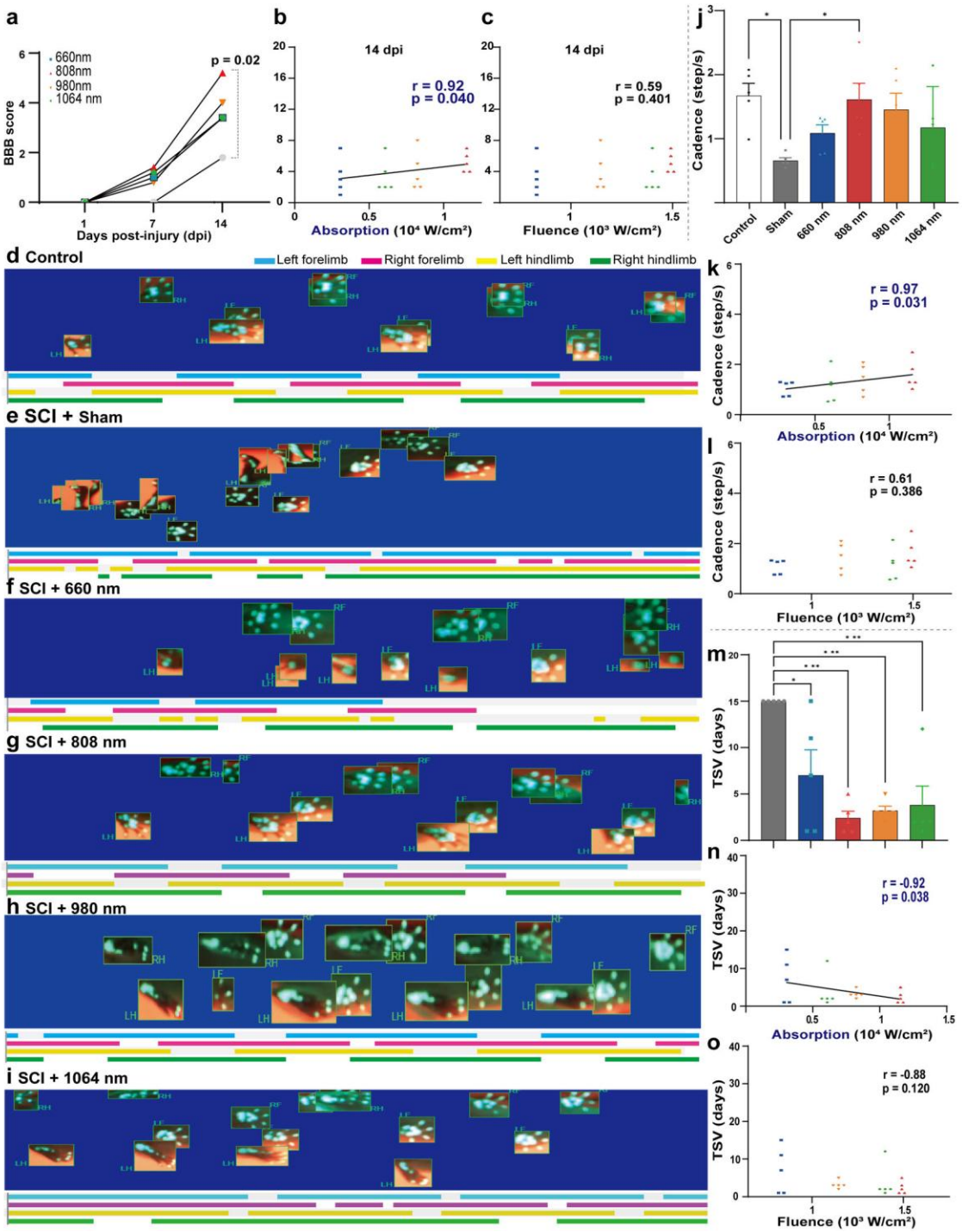

Fig. 3 | Functional recovery and its association with target-tissue optical metrics. (a) BBB scores in Sham and PBM-treated SCI groups. (b,c) Correlations between 14 dpi BBB score and spinal cord absorption or fluence. (d-i) Representative CatWalk gait patterns and step sequences. (j) Cadence at 14 dpi, used as the primary gait endpoint for optical correlation analysis. (k,l) Cadence correlations. (m) Time to spontaneous voiding (TSV).

(n,o) Correlations with TSV. Data are mean ± s.e.m. In correlation panels, individual points indicate biological variability, while Pearson r and P values were calculated based on the four wavelength-level group means. Multiple-testing-adjusted results are provided in Supplementary Table 31.

Histological outcomes and absorbed optical exposure

H&E sections showed lesion cavities and hemorrhagic injury after SCI, with different degrees of tissue preservation among PBM-treated groups (Fig. 4a). We used lesion volume and hemorrhage area to compare the two optical descriptors against tissue damage (Fig. 4b,d).

Across the three post-injury stages, lesion and hemorrhage measures were generally lower in conditions with greater computed absorption (Fig. 4c,e). The corresponding fluence correlations were weaker. Although several absorption correlations met nominal significance thresholds, none survived the global or H&E-domain FDR adjustments.

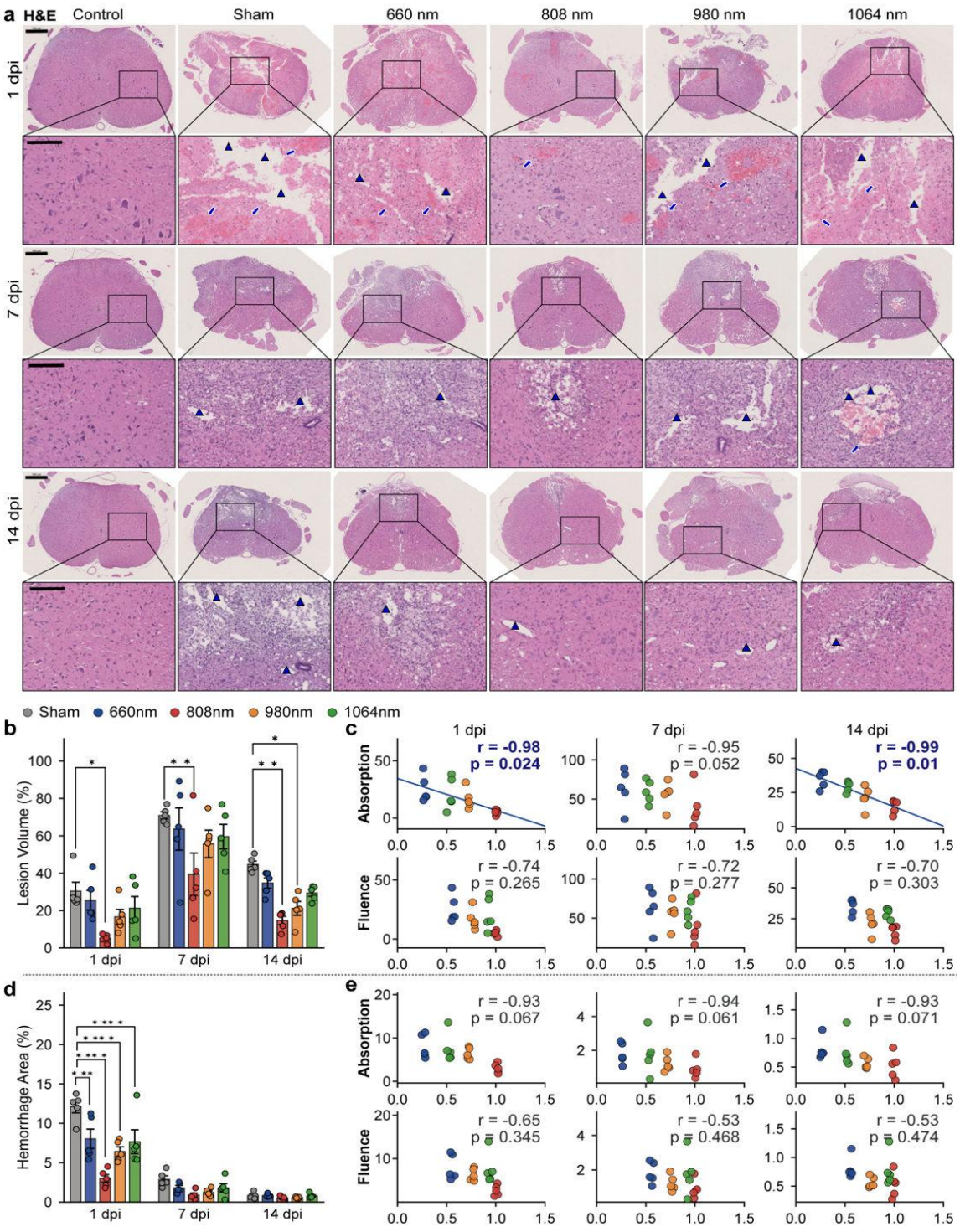

Fig. 4 | Histological damage and its association with target-tissue optical metrics. (a) Representative H&E-stained sections from Sham and PBM-treated SCI groups at 1, 7 and 14 dpi. Blue triangles indicate injury cavities, and blue arrows indicate hemorrhage foci. (b,d) Lesion volume and hemorrhage area. (c,e) Correlations with spinal cord absorption

or fluence. Data are mean ± s.e.m. In correlation panels, individual points show biological variability, whereas Pearson r and P values were computed from the four wavelength-level group means. Scale bars are indicated. Multiple-testing-adjusted results are provided in Supplementary Table 31.

Neuronal readouts associated with target absorption

Nissl staining showed changes in neuronal morphology and in positive-cell count, mean soma area and integrated optical density (IOD) across groups and time points (Fig. 5). These measures were more closely correlated with absorption than with fluence. All nine Nissl associations survived the exploratory domain-wise FDR adjustment, although none remained significant after global correction.

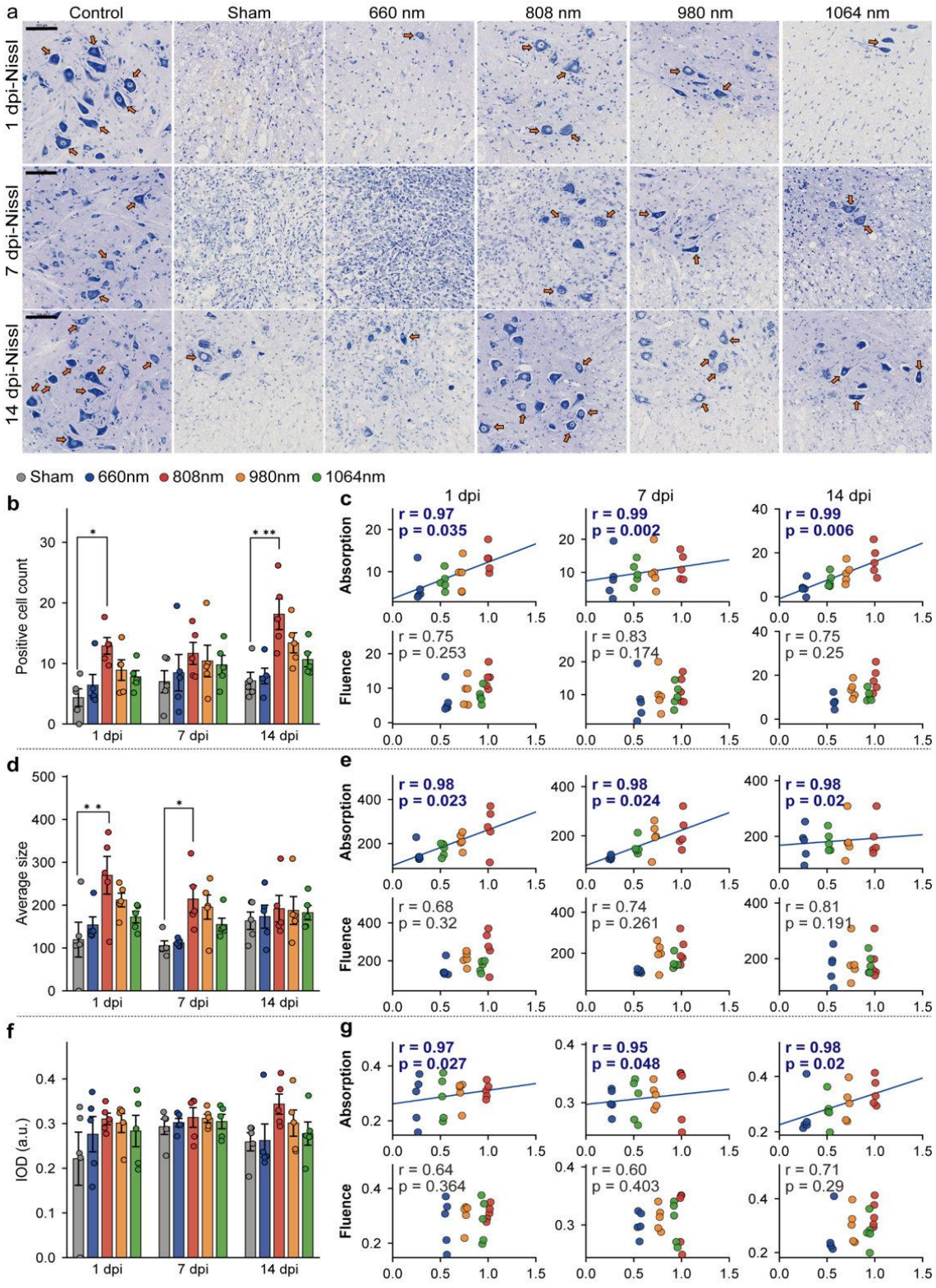

Fig. 5 | Nissl-based neuronal measurements and their optical associations. (a) Representative Nissl-stained sections from Sham and PBM-treated SCI groups at 1, 7, and

14 dpi. Orange arrows indicate representative Nissl-positive neuronal morphology. (b,d,f) Quantitative analyses of Nissl-positive cell count, soma area, and IOD. (c,e,g) Correlations of the above metrics with spinal cord absorption or fluence; the x-axes denote corresponding wavelength-level computed optical parameters. Data are presented as mean ± s.e.m. In correlation panels, individual points reflect biological variability, while Pearson's r and P values were calculated based on four wavelength-level group means. Scale bar, 100 μm. Multiple-testing-adjusted results are provided in Supplementary Table 31.

NeuN immunofluorescence provided a second set of neuronal structural measurements (Fig. 6). NeuN-positive count, mean cell size and IOD showed predominantly stronger associations with absorption than with fluence across the three time points. Four NeuN associations remained significant after domain-wise FDR adjustment, but none after global correction.

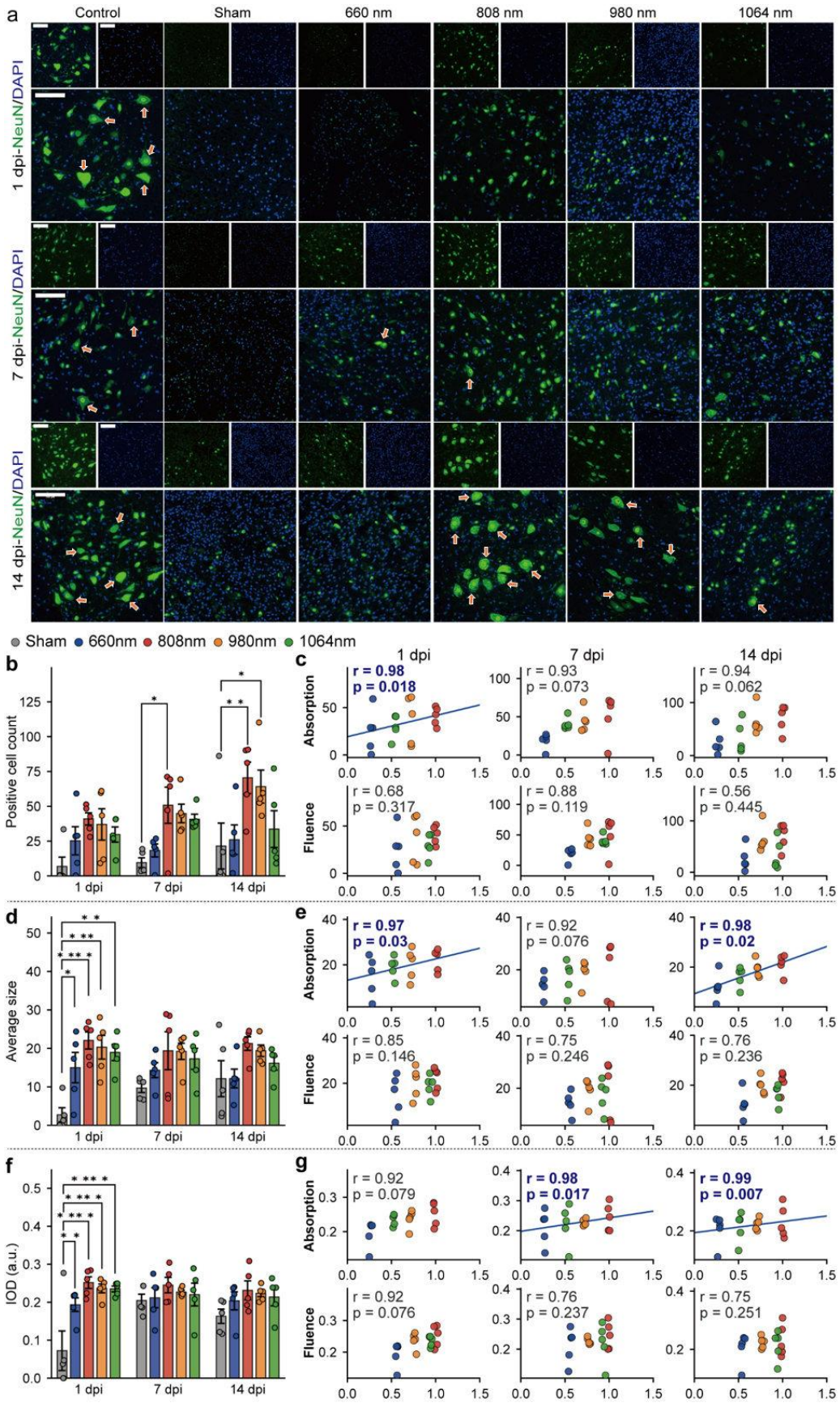
a
Control
Sham
660 nm
808 nm
980 nm
1064 nm
1 dpi-NeuN/DAPI
7 dpi-NeuN/DAPI
14 dpi-NeuN/DAPI
Sham 660nm 808nm 980nm 1064nm
b
Positive cell count
1 dpi
7 dpi
14 dpi
c
1 dpi
7 dpi
14 dpi
Absorption
Fluence
r = 0.98
p = 0.018
r = 0.93
p = 0.073
r = 0.94
p = 0.062
r = 0.68
p = 0.317
r = 0.88
p = 0.119
r = 0.56
p = 0.445
d
Average size
e
r = 0.97
p = 0.03
r = 0.92
p = 0.076
r = 0.98
p = 0.02
r = 0.85
p = 0.146
r = 0.75
p = 0.246
r = 0.76
p = 0.236
f
IOD (a.u.)
g
r = 0.92
p = 0.079
r = 0.98
p = 0.017
r = 0.99
p = 0.007
r = 0.92
p = 0.076
r = 0.76
p = 0.237
r = 0.75
p = 0.251

231

Fig. 6 | NeuN-derived structural measurements and their optical associations. (a) Representative NeuN/DAPI immunofluorescence images from sham and PBM-treated SCI groups at 1, 7, and 14 dpi. Orange arrows indicate representative NeuN-positive neuronal morphology. (b,d,f) Quantitative analyses of NeuN-positive cell count, cell size, and IOD. (c,e,g) Correlations of the above metrics with spinal cord absorption or fluence; the x-axes denote corresponding wavelength-level computed optical parameters. Data are presented as mean ± s.e.m. In correlation panels, individual points reflect biological variability, while Pearson's r and P values were calculated based on four wavelength-level group means. Scale bar, 100 μm. Multiple-testing-adjusted results are provided in Supplementary Table 31.

Vascular readouts associated with target absorption

CD31 staining was used to assess vascular-associated structural changes (Fig. 7). Positive-object count, mean size and IOD were correlated with the computed optical quantities. Absorption generally showed the stronger association, including two CD31 comparisons that survived the exploratory domain-wise FDR adjustment. CD31 morphology does not directly measure tissue perfusion or barrier function.

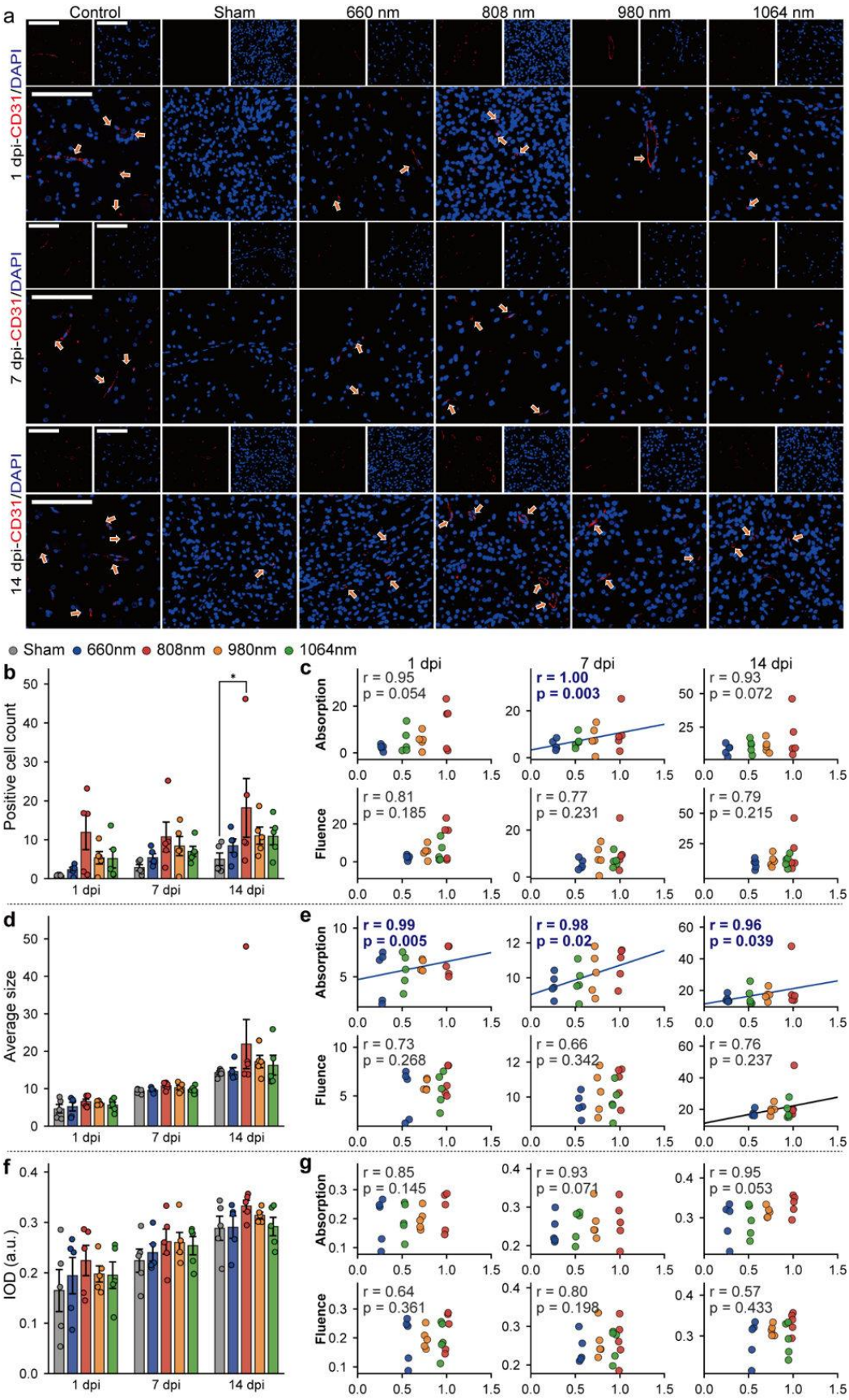
a
Control
Sham
660 nm
808 nm
980 nm
1064 nm
1 dpi-CD31/DAPI
7 dpi-CD31/DAPI
14 dpi-CD31/DAPI
Sham 660nm 808nm 980nm 1064nm
b
Positive cell count
1 dpi
7 dpi
14 dpi
c
1 dpi
7 dpi
14 dpi
Absorption
Fluence
r = 0.95
p = 0.054
r = 1.00
p = 0.003
r = 0.93
p = 0.072
r = 0.81
p = 0.185
r = 0.77
p = 0.231
r = 0.79
p = 0.215
d
Average size
e
r = 0.99
p = 0.005
r = 0.98
p = 0.02
r = 0.96
p = 0.039
r = 0.73
p = 0.268
r = 0.66
p = 0.342
r = 0.76
p = 0.237
f
IOD (a.u.)
g
r = 0.85
p = 0.145
r = 0.93
p = 0.071
r = 0.95
p = 0.053
r = 0.64
p = 0.361
r = 0.80
p = 0.198
r = 0.57
p = 0.433

248

Fig. 7 | Vascular structural measurements and their optical associations. (a) Representative CD31/DAPI images from Sham and PBM-treated SCI groups at 1, 7 and 14 dpi. Orange arrows indicate CD31-positive blood vessels. (b,d,f) CD31-positive vessel count, vessel size and IOD. (c,e,g) Correlations with spinal cord absorption or fluence. Data are mean ± s.e.m. In correlation panels, individual points reflect biological variability, while Pearson r and P values were computed from the four wavelength-level group means. Scale bar, 100 μm. Multiple-testing-adjusted results are provided in Supplementary Table 31.

Across the 37 evaluable endpoint-by-time-point comparisons, absorption had the larger absolute Pearson correlation in 35 cases (mean $|r|$ = 0.945 versus 0.718 for fluence; Supplementary Table 33). These outcomes are related measurements from the same experimental design, not 37 independent tests of optical dose. No individual association survived global Benjamini–Hochberg FDR correction. The exploratory domain-wise adjustment retained 15 absorption associations (nine Nissl, four NeuN and two CD31) and no fluence associations; none of the functional or H&E comparisons survived the domain-wise adjustment. The results indicate a consistent descriptive pattern across outcome categories.

Integrated repair and sensitivity to outcome domain

We next combined the biological endpoints into a cross-time Composite Repair Index (Fig. 8). After orienting each measure so that a higher value indicated more favorable recovery, we standardized the group means across the four illumination conditions. The invariant BBB score at 1 dpi was excluded. The remaining 37 components were averaged without weighting (Fig. 8a,b). The index was highest for the 808 nm condition and lowest for 660 nm.

The Composite Repair Index was strongly correlated with computed absorption (r = 0.998; exact one-sided permutation P = 0.042), compared with r = 0.758 for fluence (P = 0.125; Fig. 8c,d). With four conditions, P = 0.042 is the smallest attainable one-sided exact permutation value. Principal-component analysis yielded a similar descriptive ordering (Fig. 8e). In a sensitivity analysis using rounded group means from the Supplementary Information, the absorption correlation remained stronger after removing each outcome

domain in turn (approximately r = 0.992–1.000 for absorption and 0.742–0.778 for fluence).

As an external exploratory comparison, we digitized the published multi-wavelength traumatic brain injury (TBI) data of Wu et al.[22] and related neurological recovery to literature-constrained optical estimates (Fig. 8f–h). Absorption again showed the stronger directional association. Because this reanalysis uses published group-level trajectories, approximate tissue optics and a different injury model, it should be viewed as a sensitivity observation rather than an independent prospective validation or a demonstration of causal generalizability.

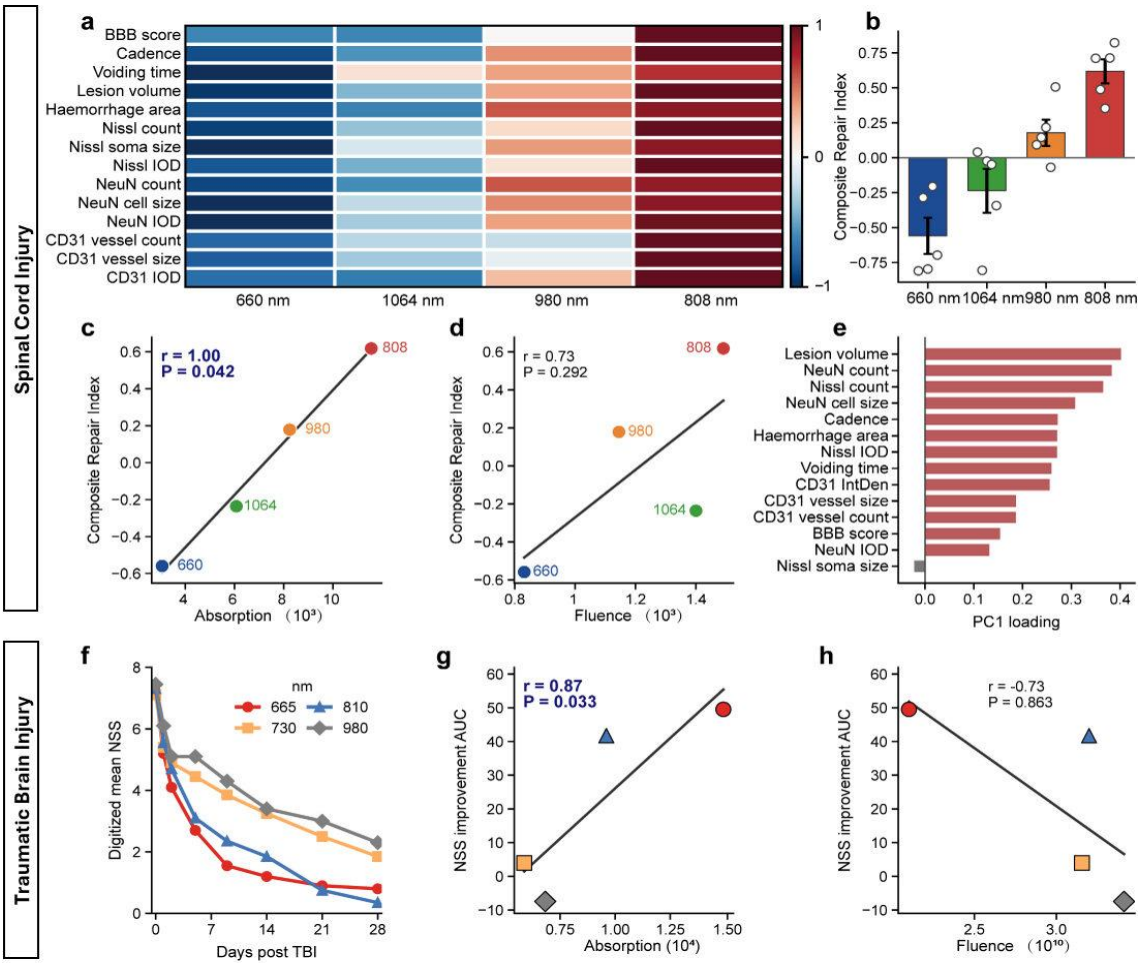

Fig. 8 | Integrated repair outcomes and comparison of target-level optical metrics. (a) Direction-aligned cross-time phenotype z-score heat map for functional, histological, neuronal structural, and vascular endpoints. Higher values indicate a more favorable endpoint direction; adverse endpoints were sign-reversed prior to standardization.

Wavelengths are ordered by voxel-summed spinal cord photon absorption. (b) Cross-time Composite Repair Index. (c,d) Associations of the index with spinal cord absorption and fluence; Pearson r and exact one-sided permutation P values were calculated from the four illumination-level values, with P = 0.042 corresponding to the minimum testable value for this sample size. (e) PC1 loadings for individual endpoints. (f) Digitized neurological severity score (NSS) trajectories from an independent multi-wavelength TBI dataset. (g,h) Associations of NSS improvement area under the curve (AUC) with brain absorption and fluence, computed from wavelength-level values. Symbols denote wavelengths.

Discussion

As PBM technologies advance toward clinical application, accurate delivery of light to a chosen target is necessary but insufficient for precise, reproducible treatment. Existing computational studies have substantially improved fluence-based estimation and treatment planning: Yaroslavsky et al. used mucosal fluence rate to calculate extraoral exposure times despite also reporting absorbed-power distributions;[9] Chang et al. improved predictions of brain-region fluence rate, while Zhang et al. and Girasol et al. used fluence to evaluate illumination sites, power ratios and beam geometry.[10-12] Other studies have assessed device transmission and fluence,[13] brain-region energy accumulation,[14] and spinal cord fluence and absorption,[21] but their relative associations with matched biological outcomes remain unresolved.

The primary finding is that absorption was associated more consistently with recovery across the tested optical conditions. It had the larger absolute correlation in 35 of 37 evaluable endpoint-by-time-point comparisons, spanning locomotion and bladder function, lesion and hemorrhage measures, and neuronal and vascular readouts. Absorption also showed stronger correspondence with the cross-time Composite Repair Index. These findings support absorption as a candidate biological dose descriptor under the conditions tested; its predictive accuracy and applicability beyond these conditions require prospective validation.

The second contribution is a practical means of obtaining the candidate descriptor. Using the segmented anatomy and tissue optical properties, the voxel model tracks

wavelength-specific photon transport, assigns absorption to the tissues traversed and integrates the absorption output within a defined spinal cord ROI. The resulting metric is a relative estimate of bulk tissue absorption; it is neither a calibrated absorbed-energy dose nor a measure of absorption by individual chromophores. This distinction matters because biological photoreception involves specific absorbers, while the calculated bulk absorption also includes energy deposited elsewhere in the tissue.[15,18-20] The present framework therefore links an internal optical estimate to measured repair without claiming to measure the molecularly effective dose.

Fluence remains essential for determining whether illumination reaches a target and for characterizing its local optical field. However, improving the accuracy of light delivery or model prediction does not automatically identify the quantity that should be controlled to obtain reproducible biological effects. Our data support further testing of tissue absorption as a descriptor linking optical exposure to repair. For translation, a biologically informative target-dose metric is needed to guide prospective dose adjustment alongside accurate source calibration. Molecular photoacceptor effects and other photobiological pathways can further vary with treatment parameters and tissue composition,[24] so bulk absorption should be evaluated alongside fluence. Prospective comparisons that separately control fluence and absorption will be needed before either can be prescribed as a validated biologically effective target dose.

The spinal cord injury model provides an optically demanding setting for evaluating the broader question of dose-metric selection. Injury to this deep target entails interconnected neuronal, inflammatory and vascular changes that can be evaluated alongside functional recovery.[25-28] Experimental SCI studies have reported neurological or tissue-level improvements after PBM and explored mitochondrial, immune and transcriptional response pathways.[29-34] Stevens et al. matched implantable and transcutaneous light exposure at the spinal cord and measured neuroregeneration and recovery, but did not directly compare fluence with local absorption.[35] Recent experimental studies reported additional functional and structural benefits, while reviews highlight the variation in SCI-PBM protocols and the unresolved issue of target-level dose standardization.[36-39] The recent movement of SCI-PBM into clinical evaluation makes this question more pressing, but clinical outcomes alone cannot establish the most biologically

353 informative internal optical metric.[40] Other mechanistic studies further illustrate the
354 complexity of the response pathways, leaving the dose-metric comparison unresolved.[41]
355 The present work extends these studies by linking two model-derived quantities from the
356 same anatomical ROI to matched biological readouts.

357 The agreement across outcome domains strengthens the descriptive observation,
358 although several measurements were made on related tissues and all correlations use the
359 same four optical conditions. The Composite Repair Index and leave-one-domain-out
360 analyses indicate that the overall pattern was not driven by a single outcome category; they
361 do not provide additional independent exposure conditions or establish the predictive
362 superiority of absorption.

363 The main limitation is that the four optical conditions were generated by changing
364 wavelength, which affects photoacceptor spectra as well as tissue propagation and
365 absorption. The data therefore cannot isolate bulk absorption as the cause of recovery. The
366 optical model also used literature-derived properties, including brain-derived
367 approximations for spinal cord optical properties, static anatomy and a hematoma
368 compartment that did not vary with injury stage. The computed fields were not validated
369 against phantom or in vivo optical measurements, and uncertainty in tissue properties was
370 not propagated. The reported integrated outputs are relative quantities rather than calibrated
371 estimates of absorbed energy, and total absorption includes light captured by water, blood
372 and other non-target absorbers. Finally, the compression model and female-only cohort
373 limit generalization. Future work should vary irradiance within a fixed wavelength, test
374 absorption-matched conditions and validate both internal optical fields and biological
375 outcomes prospectively.

376 Together, these findings suggest that choosing a biologically informative internal
377 optical-dose descriptor is an essential step toward more precise and reproducible PBM. By
378 pairing anatomy-resolved Monte Carlo estimates with measured tissue and functional
379 outcomes, we found that relative target absorption was more consistently associated with
380 repair than fluence across the tested conditions. This result supports the further evaluation
381 of absorption as a candidate for future dose-control strategies, while calibrated optical
382 measurements, fixed-wavelength dose-ranging studies and independent prospective

outcome validation remain necessary before absorption-guided clinical prescription can be justified.

Materials and methods

Voxel-based optical light-transport computation

Target fluence and absorption were estimated using three-dimensional voxel-based Monte Carlo light transport in a representative rat thoracic anatomy (Fig. 1b). The computational approach builds on established photon-transport methods.[6,7,42,43] The model contained skin, adipose tissue, muscle, bone, spinal cord, hematoma and adjacent viscera. Optical properties were assigned by tissue type, using brain measurements where matched spinal cord values were unavailable.[44-46] The voxel grid measured 0.1 × 0.1 × 0.5 mm; wavelength-dependent inputs are reported in Supplementary Tables 3 and 4.

Four illumination conditions (660, 808, 980 and 1064 nm) were simulated with identical anatomical and incident-beam geometries. Fluence described the spatial availability of propagating optical energy; absorption was obtained from weight losses along photon paths with tissue absorption applied at the corresponding voxels (Supplementary Note 1). Profiles and maps were extracted in transverse, coronal and sagittal planes. Both outputs were integrated over the same predefined spinal cord ROI to compare relative target-level exposure across conditions.

Integrated ROI metrics were defined as the sum of voxel-wise light-transport output values within the segmented spinal cord region:

$$A_\lambda, ROI = \sum_{i \in \mathrm{ROI}} a_{\lambda,i} \quad (1)$$

$$F_{\lambda,\mathrm{ROI}} = \sum_{i \in \mathrm{ROI}} f_{\lambda,i} \quad (2)$$

where λ denotes illumination wavelength, and aλ,i and fλ,i are the respective absorption and fluence outputs for voxel i. These sums are *relative integrated computational outputs*, not calibrated absorbed energy (J), absorbed-energy density (J cm−3) or physical target fluence (J cm−2). Values were compared only under the common source, ROI and simulation-output normalization used for all conditions (Supplementary Table 5). A local

absorbed-power density may be expressed as μaΦ when Φ denotes fluence rate, but this relation does not convert arbitrary simulator output into an experimentally calibrated biological dose.

Voxel-wise threshold analyses were performed independently for photon absorption and fluence using log10-transformed light-transport computation outputs from the spinal cord ROI. For each optical metric, unified threshold intervals were defined based on the range of positive voxel values across all four wavelengths, and identical interval boundaries were applied consistently to each wavelength. For a given optical metric mλ,i, interval volume and cumulative coverage were calculated as follows:

$$N_{\lambda,j} = \mathrm{Count}\left[T_j \le \log_{10}\left(m_{\lambda,i}\right) < T_{j+1}\right], \quad i \in \mathrm{ROI},\ m_{\lambda,i} > 0 \tag{3}$$

$$V_{\lambda,j} = N_{\lambda,j} \times V_{\mathrm{voxel}} \tag{4}$$

$$C_{\lambda}(T) = \frac{\mathrm{Count}\left[\log_{10}\left(m_{\lambda,i}\right) \ge T\right]}{N_{\mathrm{ROI}}} \times 100\%, \quad i \in \mathrm{ROI},\ m_{\lambda,i} > 0 \tag{5}$$

where Tj and Tj+1 define the boundaries of the jth log10 intensity interval, Nλ,j indicates the number of spinal cord voxels within the corresponding interval, Vλ,j represents the matched voxel volume, and Cλ(T) denotes the cumulative fraction of spinal cord voxels above threshold T.

For each wavelength, ten light-transport runs used the same anatomy and source settings. The reported ROI metrics were averages of these simulations (Supplementary Table 3). Their purpose was numerical repeatability; repeated simulation runs did not increase the number of independent biological exposure conditions, which remained four.

Study design

We used a T10 compression SCI model to compare computed target-tissue fluence and absorption with functional, histological and immunofluorescence outcomes. Four illumination wavelengths provided distinct optical exposures under otherwise matched prescribed surface conditions.

Rats were assigned to six experimental groups: an uninjured Control group, an injured sham-irradiation group (SCI + Sham), and injured groups treated with PBM at 660, 808,

980 or 1064 nm. The uninjured Control group served as a baseline reference and was included where appropriate in the main figures. Injured animals were evaluated at 1, 7 or 14 dpi. Unless otherwise specified, each experimental subgroup included five biological replicates.

Animals were randomly allocated to experimental groups prior to surgery. Behavioral scoring, image acquisition, and quantitative image analysis were performed by investigators blinded to group allocation. Irradiation procedures were not blinded due to the physical distinguishability of wavelength-specific devices. Animals or data points were excluded only when predefined technical criteria were met: failed injury induction, non-endpoint mortality, tissue-processing failure, and insufficient image quality for quantitative analysis.

Animals

Adult female Sprague-Dawley rats aged 8 weeks with a body weight of approximately 200 g were used for all in vivo experiments. Single-sex animal usage was adopted to reduce cohort variability and ensure comparability with previous SCI-PBM studies utilizing the same model; sex-dependent biological effects were not investigated in the present work. Animals were housed under standard laboratory conditions with controlled temperature and humidity, a 12 h light-dark cycle, and ad libitum access to food and water. All experimental procedures complied with institutional guidelines for animal care and use and were approved by the Animal Care and Use Committee of the Institute of Radiation Medicine, Chinese Academy of Medical Sciences and Peking Union Medical College.

Thoracic spinal cord injury model

A thoracic spinal cord compression injury was generated at the T10 vertebral level. Anesthesia was induced using 4% inhaled isoflurane in oxygen at a flow rate of 1.0 l min^{-1} and maintained with 1.5–2.0% isoflurane at an oxygen flow of 0.5–1.0 l min^{-1}. The absence of a pedal-withdrawal reflex confirmed adequate anesthesia. A heating pad was used to maintain the body temperature throughout the surgery.

Following shaving and disinfection, a midline dorsal incision was made for exposing the thoracic vertebrae. The paraspinal muscles were dissected, and a T10 laminectomy was

performed to expose the dorsal spinal cord without dural disruption. SCI was induced by compressing the exposed T10 spinal cord for 30 s using an arterial clamp. A spacer inserted between the clamp blades established a fixed 0.5-mm compression gap (Supplementary Fig. 2). This moderate-to-severe compression model was selected for two key reasons: it yielded reproducible lesion geometry to match computed optical dose with biological outcomes, and previous SCI-PBM studies indicate that compression injuries are more susceptible to light-mediated functional and tissue modulation than contusion injuries. This model provided a reproducible proof-of-concept geometry and was not designed to recapitulate all features of clinical contusion. After compression, the clamp was removed, the surgical field was examined to confirm successful injury induction, and the muscle and skin layers were closed sequentially. Postoperative care included thermal support, daily monitoring of general health status, body weight and wound healing, and manual bladder expression until the recovery of spontaneous voiding function.

Photobiomodulation treatment

PBM began 1 h after SCI and was administered once daily for 50 min until the 1-, 7- or 14-day endpoint. The 660, 808, 980 and 1064 nm groups received the same nominal surface dose; injured sham-irradiated animals underwent the same anesthesia and positioning without active light (Supplementary Note 4). For each active group, output power was 150 mW over a 0.3 cm^2 spot, giving an irradiance of 500 mW cm^{-2} and radiant exposure of 1,500 J cm^{-2} per session (Supplementary Table 1).

Following the computation-guided delivery design, the beam was positioned over the T10 injury site. The beam was aligned consistently across animals. PBM was delivered using wavelength-specific light-emitting diode devices (Changchun Leishi Optoelectronics Technology Co., Ltd., Changchun, China): MW-GX-660/1000mW for 660 nm, MW-GX-808/2000mW for 808 nm, MW-GX-980/2000mW for 980 nm and MW-GX-1064/1000mW for 1064 nm. Output power and beam alignment were verified before each session in accordance with the manufacturer's instructions.

Behavioral assessment

Locomotor recovery was assessed using the BBB scale. Rats were placed individually in an open field. The rats were allowed to move freely. At 1, 7 and 14 days after injury,

trained observers blinded to group allocation scored hindlimb movement, weight support, paw placement, coordination and trunk stability according to standard BBB criteria.[47] The left and right hindlimbs were scored separately and averaged to generate one animal-level BBB score.

Gait was assessed using an MGT-PR gait-analysis system (Anhui Zhenghua Biological Instrument Equipment Co., Ltd., Anhui, China). Rats crossed an illuminated glass walkway while MET2000 software recorded videos. Valid runs were defined as uninterrupted crossings without stopping, turning, grooming or obvious external interference. Cadence was selected as the primary gait endpoint because it provides a stable measure of stepping rhythm in valid runs and can be aligned with BBB score and spontaneous voiding in the 14 dpi optical-dose analysis. Other gait features were considered supportive outcomes. Animal-level values were calculated from valid runs.

Bladder-related recovery was evaluated based on the time to spontaneous voiding after injury. We monitored animals postoperatively. Manual bladder expression was performed as needed until spontaneous voiding returned. We defined spontaneous voiding as urination without manual expression and without marked bladder distension during routine postoperative monitoring.

Tissue preparation

At predefined experimental endpoints, rats were deeply anesthetized and perfused transcardially with approximately 100 ml of phosphate-buffered saline, followed by approximately 200 ml of ice-cold 4% paraformaldehyde prepared in phosphate buffer. A 3-cm spinal cord segment centered on the T10 injury site was dissected and post-fixed in 4% paraformaldehyde at 4°C for 24 h. Tissue samples were dehydrated in graded ethanol solutions, cleared in xylene, embedded in paraffin, and sectioned transversely for subsequent staining and immunofluorescence assays.

H&E and Nissl staining

H&E staining was used for evaluating gross tissue damage, lesion formation and hemorrhage following SCI. Sections were deparaffinized in xylene, rehydrated through graded ethanol, and then stained with hematoxylin and eosin. Subsequently, the stained

sections were dehydrated, cleared, and mounted with neutral resin or an equivalent permanent mounting medium. Lesion areas were delineated either manually or semi-automatically on serial transverse sections. Lesion volume was estimated by integrating lesion areas across serial sections and normalizing the values to the corresponding spinal cord volume. Hemorrhage area was measured within lesion-containing regions and normalized to the total spinal cord area of the same section.

In terms of lesion volume analysis, we converted serial section areas to volume estimates by trapezoidal integration:

$$V_{\text{lesion}} = \sum_{k=1}^{K-1} \left[\frac{A_{\text{lesion},k} + A_{\text{lesion},k+1}}{2} \right] \times \Delta z_k \tag{6}$$

$$V_{\text{cord}} = \sum_{k=1}^{K-1} \left[\frac{A_{\text{cord},k} + A_{\text{cord},k+1}}{2} \right] \times \Delta z_k \tag{7}$$

$$\text{Lesion volume (\%)} = \frac{V_{\text{lesion}}}{V_{\text{cord}}} \times 100\% \tag{8}$$

where Alesion,k and Acord,k are lesion and spinal cord areas at sampling level k, Δzk denotes the distance between adjacent sampling levels, and K represents the number of sampling levels. The percentage of hemorrhage area was calculated for the respective section. It was averaged across matched sampling levels when multiple sections were analyzed:

$$\text{Hemorrhage area (\%)} = \frac{A_{\text{hemorrhage}}}{A_{\text{cord}}} \times 100\% \tag{9}$$

Nissl staining was used to evaluate neuronal structural alterations after SCI and photobiomodulation treatment. Sections were deparaffinized, rehydrated, stained with cresyl violet, differentiated as needed, dehydrated, cleared, and mounted. Nissl-positive cells were quantified in predefined, fixed-size ROIs placed in anatomically matched gray matter regions adjacent to lesions, with cavities, large vessels, tissue tears, section edges, folds, and other artifacts excluded. Identical ROI size and placement criteria were applied across groups and time points. Six ROIs were analyzed per animal, from which the Nissl-positive cell count, mean soma area, and Nissl IOD were extracted.

Immunofluorescence staining and quantification

Neuronal marker signals and vascular structure after SCI and photobiomodulation were assessed using immunofluorescence. NeuN marked neuronal structures, whereas CD31 labelled vascular structures. Paraffin-embedded sections were deparaffinized using xylene, rehydrated through graded ethanol, and subjected to heat-induced antigen retrieval within citrate buffer (10 mM sodium citrate, pH 6.0). After cooling, sections were permeabilized in Triton X-100, blocked with buffer containing normal goat serum, and incubated overnight at 4 °C with rabbit monoclonal antibody against NeuN (NeuN (PT0847R) PT Rabbit mAb, YM8306, Immunoway; 1:200) or CD31 (CD31 (PT0350R) PT Rabbit mAb, YM8207, Immunoway; 1:200). Sections next underwent incubation with fluorophore-conjugated secondary antibody, counterstaining by DAPI, followed by mounting using antifade medium.

NeuN-positive cells and CD31-positive vascular structures were quantified within matched spinal cord regions, with identical thresholding and segmentation parameters applied for all groups across each staining batch. For NeuN analyses, we measured positive-cell count, mean positive-cell size and IOD. For CD31, we obtained vessel count, mean vessel size and IOD to evaluate vascular density, morphology and total endothelial-associated fluorescence. These measurements should be regarded as structural phenotypes rather than direct readouts for any molecular pathway.

Image acquisition and quantitative analysis

Whole-section bright-field and fluorescence images were acquired using a NanoZoomer S60 digital slide scanner (Hamamatsu Photonics, Hamamatsu, Japan). H&E- and Nissl-stained sections were scanned in bright-field mode, and NeuN/DAPI and CD31/DAPI sections in fluorescence mode. Unless otherwise stated, images were captured at an equivalent magnification of ×20 with identical settings within each staining or immunofluorescence batch. Subsequently, all images were exported as TIFF files for quantitative analysis.

Images were analyzed using ImageJ/Fiji.[48] ROIs were defined anatomically and applied consistently across animals, groups, and time points. Fluorescence images underwent background correction and threshold-based segmentation following a unified

workflow within each staining batch. Positive-object count, mean object size, and IOD were extracted from each ROI. Lesion and hemorrhage areas were measured on whole-section or lesion-region H&E images. Section- or ROI-level measurements were averaged for each animal prior to group-level analysis.

For staining-based intensity measurements, IOD was defined as the sum of positive-pixel intensities within the ROI following threshold-based segmentation:

$$\mathrm{IOD} = \sum_{p=1}^{N_p} I_p \tag{10}$$

where Ip denotes the intensity of positive pixel p, and Np represents the number of positive pixels within the segmented ROI. This value is equivalent to the positive area multiplied by the mean signal intensity of the segmented signal.

Optical-dose correlation and integrated repair analysis

Integrated spinal cord absorption and fluence were evaluated as candidate optical descriptors. At each time point, each descriptor had four values—one per illumination condition—and was paired with the corresponding group mean for each functional, histological, neuronal or vascular endpoint. The same four optical values were reused across related endpoints; animals within each group were biological replicates for outcomes but did not provide additional independent optical conditions. The analysis is therefore exploratory and cannot identify a unique causal mediator.

Individual animal observations are shown in relevant scatter plots to illustrate biological variability, while Pearson correlations and associated P values were calculated only from the four illumination-level group means. The 37 evaluable endpoint-by-time-point comparisons were not independent tests: repeated measures, common anatomy and correlated outcome domains limit confirmatory inference from cross-endpoint comparisons.

A cross-time Composite Repair Index summarized the 37 non-constant endpoint-by-time-point measures after excluding the invariant 1-day BBB component. For each endpoint, adverse measures (time to spontaneous voiding, lesion volume and hemorrhage area) were sign-reversed and values were standardized across four treatment conditions.

The index for each condition was the unweighted mean of the 37 standardized components; principal-component analysis provided a descriptive cross-check (Fig. 8e). Exact one-sided permutation probabilities for associations with the index were calculated over the 4! = 24 possible input assignments. A separate leave-one-domain-out sensitivity analysis recomputed the index after removing in turn functional, H&E, Nissl, NeuN or CD31 measurements, using the group means reported in Supplementary Tables 12, 16, 19, 23 and 27; values based on tabulated rounded means were reported approximately.

For the external traumatic brain injury sensitivity analysis, NSS trajectories reported by Wu et al.[22] were digitized from the published figure. Wavelength-level recovery was quantified as the area under the control-minus-PBM NSS improvement curve across the 28-day follow-up period. The digitized dataset was used exclusively for external sensitivity analysis and was not pooled with the SCI dataset.

Statistical analysis

Data are presented as mean ± s.e.m. unless otherwise stated. Statistical analyses were performed using GraphPad Prism, MATLAB, and Origin. Comparisons covering multiple optical inputs and time points were conducted through two-way analysis of variance (ANOVA) followed by Tukey's multiple-comparison test. Selected-group comparisons were performed using one-way ANOVA with Tukey's post hoc test or unpaired t-tests, as appropriate. Normality and homogeneity of variance were assessed prior to parametric analysis.

For optical-descriptor analyses, Pearson r, two-sided nominal P values and R^2 were calculated across four condition-level means for each outcome. Fisher-z confidence intervals, Spearman ρ, Kendall τ and exact permutation analyses were reported as exploratory checks; for n = 4, the intervals are necessarily wide. The Williams test compared dependent correlations sharing the same biological endpoint (Supplementary Table 32), and no individual comparison established significant superiority of absorption.[49] Benjamini–Hochberg FDR adjustment was applied across all non-constant endpoints within each optical metric and also jointly across both metrics as a sensitivity analysis.[50] Additional domain-specific FDR results were exploratory and did not replace global correction. The paired Wilcoxon summary across endpoints (Supplementary Table 33) is

descriptive because the endpoints are correlated and reuse four optical conditions, so its nominal P value should not be treated as an independent confirmatory test.

For the external TBI sensitivity analysis, Pearson correlation was used to associate NSS improvement AUC with literature-bounded light-transport estimates of mouse-brain photon absorption and fluence. This wavelength-level analysis was interpreted as exploratory.

For the exploratory human forearm sensitivity analysis, published multichannel HbO and oxCCO responses from Pruitt et al.[23] were digitized and compared with dose-weighted absorption and fluence estimates from a simplified, literature-constrained forearm calculation. This analysis assessed directional plausibility only and did not constitute an independently collected human validation cohort.

Data availability

Group-level biological means, model-derived optical ROI outputs and numerical statistics underlying the principal comparisons are reported in the manuscript and Supplementary Tables 5 and 7–33. Additional raw data and supporting materials are available from the corresponding author upon reasonable request.

Code availability

The voxel light-transport calculations, optical-output extraction and statistical methods are described in Materials and methods and Supplementary Notes 1–3. Custom MATLAB scripts for optical-output extraction, correlation analysis and construction of the Composite Repair Index are available from the corresponding author upon reasonable request.

Funding

This work was supported by the National Key R&D Program of China (2025YFC3608500, 2025YFE0218400, 2025YFC2427800 and 2025ZD0548504), the Major Research Plan of the National Natural Science Foundation of China (92570204), and the PUMC Outstanding Talent Program (2025I2MXHJC045). Additional support was provided by the Baylor Scott & White Central Texas Foundation through the philanthropy of Drayton McLane, Jr.

Author contributions

T.L. and Z.C. conceived and designed the study. Z.C. performed modelling, animal experiments and dose–outcome analyses and drafted the manuscript. M.L. and P.W. performed histological and statistical analyses. B.Z. performed animal experiments; X.C. and T.L., optical modelling. J.J. and L.Z.L. interpreted data. F.W., E.W. and J.H.H. and T.L. performed discussion and manuscript revision. T.L. acquired funding and supervised the study. All authors reviewed and approved the manuscript.

Competing interests

The authors declare no competing interests.

Supplementary Information accompanies this manuscript as a separate submission file.

References

1. Chung, H. et al. The nuts and bolts of low-level laser/light therapy. Ann. Biomed. Eng. 40, 516-533 (2012).

2. de Freitas, L. F. & Hamblin, M. R. Proposed mechanisms of photobiomodulation or low-level light therapy. IEEE J. Sel. Top. Quantum Electron. 22, 7000417 (2016).

3. Wang, C. et al. Challenges and opportunities in next-generation LED therapeutic devices. Light Sci. Appl. 14, 319 (2025). https://doi.org/10.1038/s41377-025-01990-z.

4. Jacques, S. L. Optical properties of biological tissues: a review. Phys. Med. Biol. 58, R37-R61 (2013).

5. Cheong, W. F., Prahl, S. A. & Welch, A. J. A review of the optical properties of biological tissues. IEEE J. Quantum Electron. 26, 2166-2185 (1990).

6. Wang, L., Jacques, S. L. & Zheng, L. MCML-Monte Carlo calculation of light transport in multi-layered tissues. Comput. Methods Programs Biomed. 47, 131-146 (1995).

7. Jacques, S. L. Tutorial on Monte Carlo calculation of photon transport in biological tissues. Biomed. Opt. Express 14, 559-576 (2023).

8. Yuan, Y. et al. Transcranial photobiomodulation with near-infrared light from childhood to elderliness: simulation of dosimetry. Neurophotonics 7, 015009 (2020).

9. Yaroslavsky, A. N. et al. Monte Carlo based dosimetry of extraoral photobiomodulation for prevention of oral mucositis. Sci. Rep. 13, 20425 (2023).

10. Chang, Y.-C. et al. Noninvasive prediction of photon fluence rate in targeted brain regions for personalized transcranial photobiomodulation dosage: model development and in silico evaluation. Biomed. Opt. Express 16, 4929–4943 (2025). https://doi.org/10.1364/BOE.570066.

11. Zhang, B., Yang, S., Piao, M., Chang, P. & Li, T. Effect of incidence sites on light distribution at different wavelengths during transcranial photobiomodulation. Acad. Radiol. 33, 1767-1780 (2026). https://doi.org/10.1016/j.acra.2025.04.076.

12. Girasol, C. E. et al. Monte Carlo simulations of optical propagation in human skin using experimentally measured laser parameters. Lasers Med. Sci. 41, 109 (2026). https://doi.org/10.1007/s10103-026-04911-7.

13. Enam, S., Saint-Martin, L., Manwar, R. & Avanaki, K. Micro-CT-informed Monte Carlo and experimental dosimetry of transcranial photobiomodulation devices. Sci. Rep. (2026). https://doi.org/10.1038/s41598-026-75995-y.

14. Van Lankveld, H. et al. Simulation-based dosimetry of transcranial and intranasal photobiomodulation of the human brain: the roles of wavelength, power density and skin tone. Biomed. Opt. Express 16, 3295-3310 (2025).

15. Amaroli, A. et al. Photobiomodulation on isolated mitochondria at 810 nm: first results on the efficiency of the energy conversion process. Sci. Rep. 14, 11060 (2024). https://doi.org/10.1038/s41598-024-61740-w.

16. Huang, Y.-Y., Sharma, S. K., Carroll, J. & Hamblin, M. R. Biphasic dose response in low level light therapy – an update. Dose Response 9, 602–618 (2011). https://doi.org/10.2203/dose-response.11-009.Hamblin.

17. Su, C.-T. & Wu, J.-H. Photobiomodulation in biological tissues: light penetration, dosimetry, and potential applications. Opt. Lasers Eng. 186, 108852 (2025).

18. Karu, T. I. Primary and secondary mechanisms of action of visible to near-IR radiation on cells. J. Photochem. Photobiol. B 49, 1-17 (1999).

19. Karu, T. I. Mitochondrial signaling in mammalian cells activated by red and near-IR radiation. Photochem. Photobiol. 84, 1091-1099 (2008).

20. Poyton, R. O. & Ball, K. A. Therapeutic photobiomodulation: nitric oxide and a novel function of mitochondrial cytochrome c oxidase. Discov. Med. 11, 154-159 (2011).

21. Chen, Z., Wang, F., Yang, C., Long, H. & Li, T. Effects of wavelength and spinal cord injury segment on photobiomodulation efficacy: Monte Carlo simulation in a rat model. J. Biomed. Opt. 30, S23907 (2025). https://doi.org/10.1117/1.JBO.30.S2.S23907.

22. Wu, Q. et al. Low-level laser therapy for closed-head traumatic brain injury in mice: effect of different wavelengths. Lasers Surg. Med. 44, 218-226 (2012).

23. Pruitt, T. et al. Photobiomodulation at different wavelengths boosts mitochondrial redox metabolism and hemoglobin oxygenation: lasers vs. light-emitting diodes in vivo. Metabolites 12, 103 (2022).

24. Sharma, S. K., Sardana, S. & Hamblin, M. R. Role of opsins and light or heat activated transient receptor potential ion channels in the mechanisms of photobiomodulation and infrared therapy. J. Photochem. Photobiol. 13, 100160 (2023).

25. Ahuja, C. S. et al. Traumatic spinal cord injury. Nat. Rev. Dis. Primers 3, 17018 (2017).

26. Tran, A. P., Warren, P. M. & Silver, J. The biology of regeneration failure and success after spinal cord injury. Physiol. Rev. 98, 881-917 (2018).

27. Donnelly, D. J. & Popovich, P. G. Inflammation and its role in neuroprotection, axonal regeneration and functional recovery after spinal cord injury. Exp. Neurol. 209, 378-388 (2008).

28. Oudega, M. Molecular and cellular mechanisms underlying the role of blood vessels in spinal cord injury and repair. Cell Tissue Res. 349, 269-288 (2012).

29. Byrnes, K. R. et al. Light promotes regeneration and functional recovery and alters the immune response after spinal cord injury. Lasers Surg. Med. 36, 171-185 (2005).

30. Ando, T. et al. Low-level laser therapy for spinal cord injury in rats: effects of polarization. J. Biomed. Opt. 18, 098002 (2013).

31. da Cruz Tobelem, D. et al. Effects of photobiomodulation in experimental spinal cord injury models: a systematic review. J. Biophotonics 15, e202200059 (2022).

32. Zhu, Z. et al. Photobiomodulation promotes repair following spinal cord injury by restoring neuronal mitochondrial bioenergetics via AMPK/PGC-1α/TFAM pathway. Front. Pharmacol. 13, 991421 (2022).

33. Ma, Y. et al. Photobiomodulation attenuates neurotoxic polarization of macrophages by inhibiting the Notch1-HIF-1α/NF-κB signalling pathway in mice with spinal cord injury. Front. Immunol. 13, 816952 (2022).

34. Stevens, A. R. et al. Evaluation of transcriptomic changes after photobiomodulation in spinal cord injury. Sci. Rep. 15, 3193 (2025).

35. Stevens, A. R. et al. Implantable and transcutaneous photobiomodulation promote neuroregeneration and recovery of lost function after spinal cord injury. Bioeng. Transl. Med. 9, e10674 (2024). https://doi.org/10.1002/btm2.10674.

36. Del Campo, P. et al. Photobiomodulation (PBM) therapy for functional recovery using an experimental model of spinal cord injury in rats. J. Spinal Cord Med. 49, 307–316 (2026). https://doi.org/10.1080/10790268.2025.2488571.

37. Correia, D. C. C. et al. Therapeutic potential of photobiomodulation in early recovery after experimental spinal cord injury in rats: histological and biomechanical analysis. J. Biophotonics 19, e202500348 (2026). https://doi.org/10.1002/jbio.202500348.

38. Drew, I. K. M., Harvey, A. R., Wallace, V. P. & Hodgetts, S. I. Optimization of photobiomodulation therapy for spinal cord injury: a review. Photochem. Photobiol. 102, 797-831 (2026).

39. Yang, L. et al. Advances in the application of photobiomodulation technology in spinal cord injury rehabilitation. Exp. Neurol. 404, 115869 (2026). https://doi.org/10.1016/j.expneurol.2026.115869.

774 40. Liang, Z. et al. Effects of early photobiomodulation therapy on motor recovery in
775 patients with incomplete acute cervical spinal cord injury: a multicenter randomized
776 controlled trial. J. Orthop. Transl. 56, 101040 (2026).

777 41. Zuo, X. et al. Photobiomodulation regulates inflammation and autophagy in spinal cord
778 injury through NLRP3/Caspase-1/IL-1β pathway by targeting TLR2. Mol. Immunol. 182,
779 1–10 (2025). https://doi.org/10.1016/j.molimm.2025.03.014.

780 42. Boas, D. A., Culver, J. P., Stott, J. J. & Dunn, A. K. Three dimensional Monte Carlo
781 code for photon migration through complex heterogeneous media including the adult
782 human head. Opt. Express 10, 159-170 (2002).

783 43. Prahl, S. A., Keijzer, M., Jacques, S. L. & Welch, A. J. A Monte Carlo model of light
784 propagation in tissue. SPIE Institute Series IS 5, 102-111 (1989).

785 44. Yaroslavsky, A. N. et al. Optical properties of selected native and coagulated human
786 brain tissues in vitro in the visible and near infrared spectral range. Phys. Med. Biol. 47,
787 2059-2073 (2002).

788 45. Bashkatov, A. N., Genina, E. A., Kochubey, V. I. & Tuchin, V. V. Optical properties
789 of human skin, subcutaneous and mucous tissues in the wavelength range from 400 to 2000
790 nm. J. Phys. D Appl. Phys. 38, 2543-2555 (2005).

791 46. Soleimanzad, H., Gurden, H. & Pain, F. Optical properties of mice skull bone in the
792 455- to 705-nm range. J. Biomed. Opt. 22, 010503 (2017).

793 47. Basso, D. M., Beattie, M. S. & Bresnahan, J. C. A sensitive and reliable locomotor
794 rating scale for open field testing in rats. J. Neurotrauma 12, 1–21 (1995).
795 https://doi.org/10.1089/neu.1995.12.1.

796 48. Schindelin, J. et al. Fiji: an open-source platform for biological-image analysis. Nat.
797 Methods 9, 676–682 (2012). https://doi.org/10.1038/nmeth.2019.

798 49. Williams, E. J. The comparison of regression variables. J. R. Stat. Soc. Ser. B 21, 396–
799 399 (1959). https://doi.org/10.1111/j.2517-6161.1959.tb00346.x.

800 50. Benjamini, Y. & Hochberg, Y. Controlling the false discovery rate: a practical and
801 powerful approach to multiple testing. J. R. Stat. Soc. Ser. B 57, 289–300 (1995).
802 https://doi.org/10.1111/j.2517-6161.1995.tb02031.x.

Supplementary Files

This is a list of supplementary files associated with this preprint. Click to download.

- SupplementaryInformation.docx